Electronic Supplementary Information

A "dual-key-and-lock" DNA nanodevice enables spatially controlled multi-mode imaging and combined cancer therapy

Shuzhen Yue,[a] Jiayin Zhan,[a] Xuan Xu,[a] Junpeng Xu,*[c] Sai Bi*[b] and Jun-Jie Zhu*[a]

[a]State Key Laboratory of Analytical Chemistry for Life Science, School of Chemistry and Chemical Engineering, Nanjing University, Nanjing 210023, P. R. China

[b]College of Chemistry and Chemical Engineering, Key Laboratory of Shandong Provincial Universities for Functional Molecules and Materials, Qingdao University, Qingdao 266071, P. R. China

[c]State Key Laboratory of Pharmaceutical Biotechnology, Department of Sports Medicine and Adult Reconstructive Surgery, Nanjing Drum Tower Hospital, The Affiliated Hospital of Nanjing University Medical School; State Key Laboratory of Pharmaceutical Biotechnology, Medical School, Nanjing University, Nanjing 210093, P. R. China

*E-mail: jjzhu@nju.edu.cn (J.-J. Zhu)

*E-Mail: bisai11@126.com (S. Bi)

*E-Mail: xjp@nju.edu.cn (J. Xu)

Table of Contents

S1. Additional Experimental Procedures

Materials and Reagents. All oligonucleotides used in this work were obtained from Sangon Biotechnology Co., Ltd. (Shanghai, China). The corresponding sequences are listed in Table S1. The hydrogen tetrachloroaurate (III) tetrhydrate ($HAuCl_4 \cdot 4H_2O$), Trisodium citrate dihydrate, silver nitrate ($AgNO_3$), L-ascorbic acid (AA), tannic acid (TA) and tris(2-carboxyethyl) phosphine hydrochloride (TCEP) were purchased from Sinopharm Chemical Regent Co., Ltd. (Beijing, China). Sodium sulfite (Na_2SO_3), polyvinylpyrrolidone (PVP, average MW ~55,000), manganese chloride ($MnCl_2$), magnesium chloride ($MgCl_2$), sodium chloride (NaCl) and sodium bromide (NaBr) were provided by Sigma-Aldrich (U.S.A.). The MCF-7, HeLa and HEK-293T cells used in this study were obtained from CoBioer Biosciences Co., Ltd. (Nanjing, China). The Dulbecco's modified eagle medium (DMEM) containing fetal bovine serum (FBS) and trypsin were provided from Hyclone (Logan, USA). All chemicals were of analytical grade and used as received. The ultrapure water (18.2 MΩ·cm) was used throughout the experiments.

Instrumentations. Dynamic light scattering (DLS) analysis and the ζ potential measurements were performed on a dynamic light scatterer (Brookhaven 90Plus, USA) and Zetasizer (Malvern Instrument Ltd, UK), respectively. Absorption spectra were recorded with a UV-vis spectrophotometer (UV-2600, Shimadzu, JAP).

Preparation of HA-DSNPs. *Synthesis of Au@Ag@Au DSNPs.* First, the Au cores were prepared by reducing tetrachloroauric acid ($HAuCl_4$) with trisodium citrate. Briefly, 50 mL of $HAuCl_4$ solution (0.01%, w/w) was boiled under vigorous stirring, followed by rapid adding 1.7 mL of trisodium citrate solution (1% w/w). The solution colour changed from dark purple to wine-red within 5 min. After continuously boiling for 30 min, the obtained colloidal suspension was cooled naturally to room temperature with continuous stirring. Next, to synthesize Au@Ag NPs, the pH of the resulting AuNP dispersion was adjusted to ~8.5 using glycine-NaOH buffer (pH 12.0). A portion of 400 μL silver ammonium solution (1 mM) was quickly added to 4 mL of Au NPs. Subsequently, 1 mL of L-ascorbic acid (L-AA) solution (2 mM) was injected

into the mixture with a rate of 0.1 mL/min under continuous stirring. When the colour turned to orange red, the mixture was kept stirring for another 30 min. The mixture was further centrifuged and resuspended in 2 mL of ultrapure water. Then, a robust epitaxial deposition method was used to synthesize Au@Ag@Au DSNPs, which can effectively prevent Au@Ag@Au DSNPs from galvanic replacement and ligand-assisted oxidative etching to the Au@Ag NPs. In brief, the growth solution of Au was firstly prepared, in which 2.5 μL of $HAuCl_4$ (24 mM), 120 μL of NaOH (0.2 M) and 37.5 μL of Na_2SO_3 (5 mM) were added into 3.64 mL of ultrapure water in sequence and let stand for overnight at room temperature. Finally, 3.3 mL of H_2O, 1 mL of PVP (5 wt%, Mw 55 000), 200 μL of L-AA (0.5 M), 400 μL of NaOH (0.5 M), 3.8 mL of the above-mentioned growth solution of Au, 100 μL of Na_2SO_3 (0.1 M) and 1 mL Au@Ag NPs were mixed in a glass vial to initiate the seeded growth at 60 °C for 4 h. And the Au@Ag@Au DSNPs were collected via centrifugation and washed twice with ultrapure H_2O. The concentration of Au@Ag@Au DSNPs was determined using UV-vis absorption spectrum.

Functionalization of HA hybrids on Au@Ag@Au DSNPs. The salt-aging method was used to modify Au@Ag@Au DSNP surfaces with DNA strands. First, the thiolated Hairpins were reduced with TCEP for 1.5 h, and mixed with Aptazyme in Tris-HCl buffer (20 mM, 100 mM NaCl, pH 7.4) at a molar ratio of 1:1.5. Then the mixture was heated to 95 °C for 5 min and cooled to 25 °C for 2.5 h to form the HA hybrids. Finally, the prepared HA hybrids (0.25 μM) were added to Au@Ag@Au DSNPs (2.5 nM). After overnight incubation, phosphate buffer (0.2 M, pH 7.4) was added to the solution with a final concentration of 10 mM. Besides, the NaBr solution (2.0 M) was slowly added to the mixture to reach a final concentration of 0.5 M over 10 h, followed by incubation for another 16 h. The free DNA hybrids were removed by centrifuged (12,000 rpm, 20 min) and washed three times to obtain the HA-DSNPs.

Electrophoresis Characterization. The 12% polyacrylamide gel was prepared by mixing 2.4 mL polyacrylamide gel (40%), 4 mL H_2O, 1.6 mL 5× TBE, 56 μL APS (10%, wt%) and 8 μL TEMED. Then, 10 μL of each DNA samples was mixed with 2 μL of loading buffer, followed by injection into the prepared gel. After running at 150

V for 40 min, the gel was stained with GelRed™ Nucleic Acid Gel Stain (GoldBio, USA) for 15 min and imaged by a Gel Image System (Tanon, China).

Finite Difference Time Domain (FDTD) Simulation. The optical simulations were carried out by FDTD solutions software (Lumerical Inc., Canada). The geometric parameters were obtained using the Nano Measure 1.2 software based on TEM images, and the thickness of Ag shell and outer Au shell were set to 2 nm and 1.25 nm, respectively. The dielectric constant of gold and silver was taken from the Au-Palik in FDTD database. A 633 nm incident light was used to profile the electric field distribution. The simulation region was set to 50 × 50 nm^2 with the mesh size of 0.1 nm along each of the x-, y-, and z-directions.

Calculation of the Amount of HA Hybrids Modified on Au@Ag@Au DSNPs. FAM-labelled Hairpin was used to determine the amount of HA hybrids on each Au@Ag@Au DSNPs, in which the FAM-labelled HA-DSNPs were synthesized and collected via the above-mentioned method. Then, the products were mixed with dithiothreitol (DTT, 20 mM) and incubated overnight at room temperature to completely release the DNA strands. Afterwards, the mixture was centrifuged (12,000 rpm, 15 min) to collect its supernatant for fluorescence measurement. The obtained fluorescence intensity was further converted to the concentration of HA hybrids according to a standard linear calibration curve which was measured using known concentrations of HA hybrids under the same conditions. Finally, HA hybrids on each Au@Ag@Au DSNPs was calculated based on prior knowledge of HA hybrid concentration.

Loading Content of Dox on HA-DSNPs. Different amounts of HA-DSNPs probes were mixed with 4 μL of Dox (20 μM) at the molar ratios from 1:200 to 1:8000, and the final volume of reaction system was supplemented to 80 μL with Tris-HCl buffer. After incubation at 25 °C for 24 h, the fluorescence from Dox was recorded using a F-320 fluorescence spectrometer (Tianjin Gangdong Technology Co., LTD, China) with the excitation wavelength at 488 nm.

Stability of DKL-DND. The prepared DKL-DND was co-incubated with 1× PBS (pH 7.4) and 1× PBS containing 1 U/mL DNase I for different times, respectively.

Then, the time-dependent fluorescence signal from Rox-labelled Aptazyme and Cy5-labelled Fuel strand was recorded to test the stability of DKL-DND.

pH-Responsive Ability of DKL-DND. The DKL-DND were dispersed in 1× PBS buffer (pH 7.4 or 5.5) and incubated for different time points at 37 °C (Mn equiv 0.1 mg/mL). The supernatant was collected through centrifugation and the biodegradability of DKL-DND was evaluated via monitoring the Mn^{2+} release using ICP-AES (Perkin Elmer, USA).

***In Vitro* FL/SERS Detection.** *Fluorescence detection.* To demonstrate the feasibility of DKL-DND for miR-21 detection, different reaction systems applying DKL-DND, DKL-DND + miR-21, DKL-DND + ATP, and DKL-DND + ATP + miR-21 were incubated in Tris-HCl buffer (pH 5.5) at 37 °C for 3 h, respectively. The final concentrations of DKL-DND, ATP and miR-21 were 2.5 nM, 5 mM and 50 nM, respectively. For *in vitro* miR-21 analysis, miR-21 at different concentrations (0 pM, 250 pM, 500 pM, 1 nM, 2.5 nM, 5 nM, 10 nM, 50 nM, and 75 nM) were incubated with the mixture of DKL-DND (2.5 nM) and ATP (5 mM) under the same reaction conditions as above. For selectivity analysis, the solution containing different analytes, such as target miR-21 (50 nM), one-base mismatched miR-21 (50 nM), three-base mismatched miR-21 (50 nM), miR-155 (50 nM), and the mixture of those microRNAs (50 nM) were added into the reaction system containing DKL-DND (2.5 nM) and ATP (5 mM) under acidic pH condition, followed by incubation for 3 h at 37 °C, respectively. A F-320 fluorescence spectrometer was used to record the fluorescent spectra of Rox and Cy5. The excitation wavelength of Rox was set as 587 nm, and the emission spectra were collected between 595 and 630 nm. The excitation wavelength of Cy5 was set as 635 nm, and the emission spectra were collected between 650 and 750 nm.

SERS detection. After 3 h incubation, the resulting products were centrifuged and washed twice with 1× PBS (12,000 rpm, 15 min) and dispersed in 3 μL of 1× PBS for SERS measurement. Finally, the SERS spectra were recorded using a Raman spectrometer (Renishaw inVia-Reflex, UK) with a 633 nm laser. The laser power and

accumulation were set as 100% and 10, respectively. Three spectra were collected from different locations of each sample and averaged to obtain the final data.

Cell Culture. The MCF-7, HeLa, and HEK-293T cell lines were cultured in DMEM medium containing 10% fetal calf serum, 100 mg/mL of penicillin and 100 mg/mL of streptomycin and maintained at 37 °C under humid atmosphere containing 5% CO_2. The cells were plated at the logarithmic growth phase prior to each experiment.

Flow Cytometry Analysis. An amount of 2×10^5 MCF-7 cells were seed in a 12-well plate and cultured for 24 h, followed by incubation with DKL-DND for different time points. Then, MCF-7 cells were trypsinized and washed with 1× PBS for three times by centrifugation (800 rpm, 5min). The collected cells were dispersed in 500 μL 1× PBS buffer and analyzed on a flow cytometry (Beckman Coulter FC500).

qRT-PCR Analysis. An amount of 5×10^5 MCF-7 cells were seed in a 6-well plate and cultured for 24 h, followed by incubation with PBS, N-DKL-DND and A-DKL-DND for additional 48 h, respectively. After washing with 1× PBS for three times, the total RNA from those cells were extracted using UNlQ-10 Column Total RNA Purification Kit (Sangon Biotech, Shanghai) according to the manufacturer's instructions. Subsequently, the qRT-PCR analysis was performed using BeyoFast™ SYBR Green One-Step qRT-PCR Kit (Beyotime Biotechnology, Shanghai). The mRNA expression level was evaluated via the $2^{-\Delta\Delta Ct}$ method.

Western Blot Assay. An amount of 5×10^5 MCF-7 cells was seed in a 6-well plate and cultured for 24 h. After that, the cells were treated with PBS, N-DKL-DND and A-DKL-DND for another 48 h, respectively. The final concentration of DKL-DND was 5 nM. The cells were collected and washed three times with 1× PBS, followed by lysis using RIPA lysis buffer (Sevicebio, G2002) containing 1 mM protease inhibitor (PMSF, KeyGEN BioTECH, KGB5105-10). For tumor samples, the excised tumors from mice in different treatment groups were washed with cold PBS, followed by homogenized and lysed on ice using RIPA lysis buffer containing protease inhibitor. After centrifugating at 4 °C for 15 min, the supernatants containing proteins were collected. Then, the total protein concentrations were qualified using BCA protein assay kits (Beyotime, P0012S). The obtained proteins were separated by SDS-PAGE

(Beyotime, P0052A) and further transferred to a polyvinylidene fluoride (PVDF) membrane. The membrane was blocked by a blocking solution (Beyotime, P0252) for 1 h. Washed with 1× PBST buffer three times, the membrane was successively incubated with the primary antibody against EGR-1 (Boster Biological Technology, PA2177) overnight at 4 °C and the corresponding HRP-labelled secondary antibody (KeyGEN BioTECH, KGC6202) for 1 h at room temperature. Finally, the images were obtained via a chemiluminescence image system.

Cytotoxicity Assay. To evaluate the cytotoxicity of the prepared nanodevices, 100 μL of MCF-7 cells were seeded in a 96-well plate with the density of 10^4 cells per well and incubated at 37 °C for 24 h. Then, the cells were treated with different nanodevices for 48 h, respectively. After incubation, the supernatant medium was completely removed and the cells were cultured in 100 μL of DMEM medium containing 10 μL of Cell Counting Kit-8 solution (CCK-8) (APExBIO Technology LLC, USA) for another 1.5 h. Finally, the absorbance at 450 nm of each well was measured on a microplate reader (BioTek, USA) to calculate the cell viability (%) according to the following formula:

$$\text{Cell viability (\%)} = \frac{A_{\text{treated}} - A_{\text{blank}}}{A_{\text{control}} - A_{\text{blank}}} \times 100\%$$

in which A_{blank}, A_{control}, and A_{treated} represent the absorbance of DMEM, MCF-7 cells treated with Tris-HCl buffer, and MCF-7 cells treated with different samples, respectively.

Live/Dead Cell Staining Assay. The MCF-7 cells were seeded in a confocal dish at the density of 10^5 cells and cultured at 37 °C for 24 h. Then, the medium was removed and the cells were treated with fresh DMEM containing PBS, N-DKL-DND, A-DKL-DND, free Dox, D-DKL-DND and DKL-DND, respectively. The final concentration of DKL-DND was 5 nM. After additional 48 h incubation, the cells were washed with 1× PBS three times and incubated with Calcein-AM/PI double staining kit (Beyotime Biotechnology, Shanghai) for 30 min according to the manufacturer's protocol. Subsequently, the cells were imaged by CLSM, in which the live cells emitted green fluorescence, and the dead cells emitted red fluorescence.

Mouse Tumour Model. All animal experiments were approved by the Jiangsu Animal Care and Use Committee (SYXK(Su) 2019-0056). To build the orthotopic MCF-7 tumor model, the female BALB/c nude mice (4-5 weeks old) were obtained from Nanjing Zhonghua Biotechnology Co., LTD and allowed to acclimate in the laboratory for one week. Then, 10^7 MCF-7 cells in 150 μL of PBS were injected into the right lower flank of mice. *In vivo* experiments were further carried out when the tumor grew to a certain volume. The tumor volume (V) was calculated via the following equation: $V = (Length \times Width^2)/2$.

Fluorescence Imaging *In Vivo*/*Ex Vivo*. When the tumor volume grew to ~150 mm^3, MCF-7 tumor-bearing mice were injected with Cy5-labelled Fuel strand or DKL-DND via tail vein injection method. Then the whole body imaging was carried out at each certain points (0, 4, 8, 12 and 24 h) after injection by a IVIS Lumina XRMS Series III (PerkinElmer, USA). In addition, the main organs (heart, liver, spleen, lungs, and kidney) and tumors were excised from the sacrificed mice and imaged after injection for 24 h.

T1-Weighted MRI. For *in vitro* MRI analysis, the DKL-DND with different concentrations (Mn equiv 0, 0.0625, 0.125, 0.25 and 0.5 mM.) were dispersed in 1× PBS buffer (pH 7.4 or 5.5) and incubated for 4 h at 37 °C. After centrifugation, T1-weighted images of supernatant were taken by a 1.0 T magnetic resonance equipment. The corresponding relaxation time (T1) of DKL-DND were recorded and the r1 relativity values were obtained via the curve fitting of 1/T1 versus Mn^{2+} concentration. For *in vivo* MRI analysis, MCF-7 tumor-bearing mice were injected with DKL-DND via tail vein when the tumor volume grew to ~150 mm^3. Then, the MR images were collected at 0 and 12 h post injection, respectively.

Hemolysis Assay. The fresh mouse blood was centrifuged and washed with 1× PBS three times (1500 rpm, 5 min). Then, the isolated red blood cells were diluted with 1× PBS to 10% (v/v) suspension, followed by incubation with an equal volume of water, PBS, or N-DKL-DND at different concentrations (1, 2.5, 5, 10, 15 and 20 nM) at 37 °C for 1.5 h. Those samples were successively centrifuged to remove red blood cells (1500 rpm, 5 min) and N-DKL-DND (13500 rpm, 15 min). Finally, the absorbance at

540 nm of supernatant was measured using a full wavelength reading instrument (ThermoFisher Scientific, USA). Finally, the hemolysis ratio was calculated by the following equation:

$$\text{Hemolysis (\%)} = \frac{A_{Sample} - A_{PBS}}{A_{Water} - A_{PBS}} \times 100\%$$

where A_{Sample} represents the absorbance of supernatant treated with N-DKL-DND, A_{PBS} and A_{Water} represent the absorbances of supernatant treated with PBS and H_2O, respectively.

Tissue Biodistribution of DKL-DND. The MCF-7 tumor-bearing mice were injected with DKL-DND via tail vein, and then euthanized at different time points (3, 6, 12, 24 and 48 h). Subsequently, the tumors and major organs (heart, liver, spleen, lung, and kidney) of each mouse were excised and dissolved in aqua regia for ICP-MS analysis (Inductively Coupled Plasma Mass Spectrometer, NexION 2000, PerkinElmer).

S2. Supplementary Results and Discussion

S2.1. Optimization of Ag Shell Thickness

A series of Au@Ag NPs with different Ag shell thickness were prepared. First, the deposition of Ag shell on Au NPs was characterized by TEM (Fig. S1). The average size of Au is ~17 nm (Fig. S1A-a). With the increasing concentration of silver ammonium solution from 200 to 800 mM, the average diameter of Au@Ag NPs gradually increases (Fig. S1A-b-S1A-e). The average sizes of Au@Ag_x NPs in TEM are determined as 20.08 nm (Au@Ag_{200} NPs), 21 nm (Au@Ag_{400} NPs), 22.35 nm (Au@Ag_{600} NPs) and 22.7 nm (Au@Ag_{800} NPs) respectively, in which the Ag shell thicknesses of Au@Ag_x NPs can be calculated as 1.54 nm, 2 nm, 2.28 nm and 2.85 nm, respectively. Then, the optical property of these synthesized nanoparticles was analyzed via UV-vis absorption spectra (Fig. S1B). The pure Au exhibits a prominent plasmonic absorption at 518 nm (curve a), whereas it appears two different absorption peaks relative to Au core and Ag shell after addition of silver ammonium solution with different concentrations (curves b-e). With the increasing Ag shell thickness, the maximum absorption wavelength of Au core is gradually blue-shifted to 481 nm and attenuated, and the plasmonic absorption of Ag shell at 395 nm increases at the same time.

The thickness of Ag shell has a marked impact on the SERS intensity of Au@Ag NPs. To obtain the highest Raman enhancement effect, the SERS intensities of Au@Ag NPs with different Ag shell thickness were measured, in which 4-MBA with the characteristic peak of 1590 cm^{-1} was chosen as the Raman reporter molecule. From Fig. S1C and S1D, the SERS intensity of Au@Ag NPs is enhanced significantly when the concentration of silver ammonium solution increases from 200 to 400 mM (the thickness of Ag shell is about from 1.54 to 2 nm). And the SERS intensity of Au@Ag NPs with 400 mM silver ammonium solution is ~17.5-fold than that of pure Au, indicating the wide and strong plasmon resonance of Au@Ag NPs produce a higher enhancement effect than that of pure Au NPs. However, with further increasing amount of silver ammonium solution, the SERS intensity of Au@Ag NPs decreases.

This is because the thickness of Ag shell affects the electromagnetic enhancement between Au core and Ag shell, and the Ag shell resonance gradually become dominant. Meanwhile, the thicker Ag shell might enhance the instability of Au@Ag NPs, which also has an impact on Raman enhancement effects. Therefore, the preparation of Au@Ag NPs using 400 mM silver ammonium solution (the thickness of Ag shell is ~2 nm) is chosen for further studies.

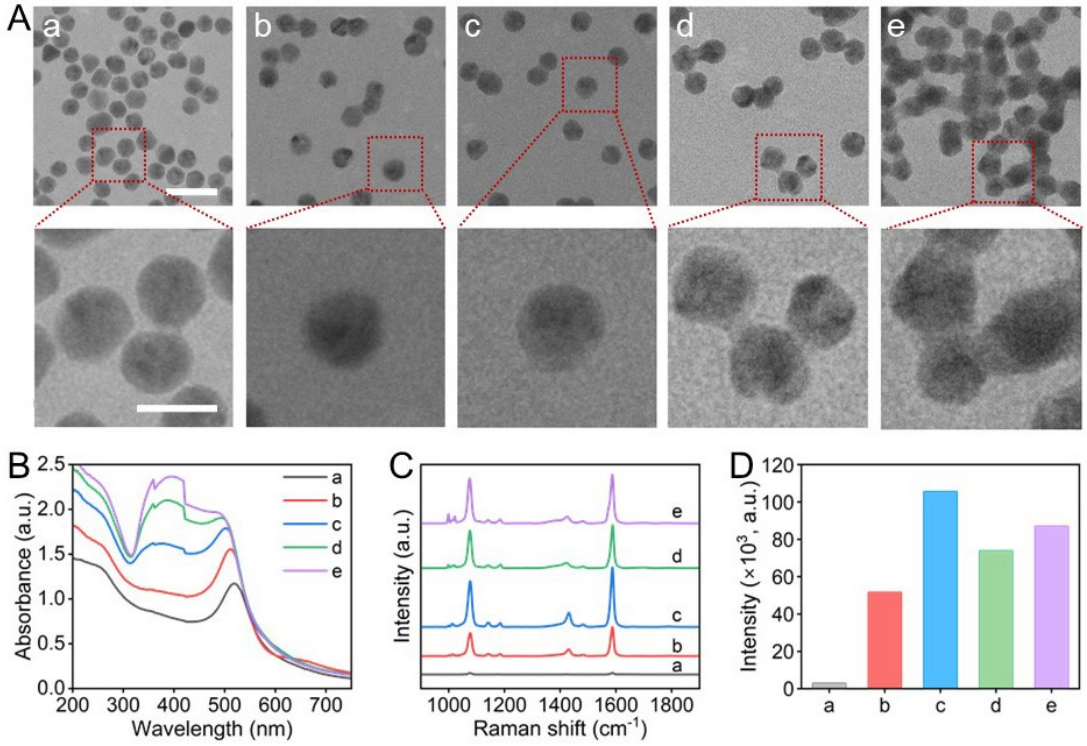

Fig. S1. (A) TEM images, (B) UV-vis absorption spectra and (C) SERS spectra of (a) Au NPs and Au@Ag NPs prepared by silver ammonium solution with different amounts of (b) 200 mM, (c) 400 mM, (d) 600 mM, and (e) 800 mM. (D) Corresponding SERS intensities from (C). The scale bars in (A) and the enlarged images are 50 nm and 20 nm, respectively.

S2.2. Optimization of Au Shell Thickness

An Au shell is further coated on Au@Ag NPs to form the Au@Ag@Au DSNPs, and the thickness of outer Au shell plays an important role in constructing the double-shelled SERS substrate. In brief, the insufficient thickness of Au shell cannot protect Ag layer from etching under the harsh treatments such as hydrogen peroxide (H_2O_2), while coating Ag with over thickened Au will affect the plasmonic properties of Au@Ag@Au DSNPs. Thus, the Au shell thickness was optimized via a series of characterization experiments. The Au@Ag@Au DSNPs presents a homogeneous and well monodispersed spherical morphology (Fig. S2A). Moreover, with the increasing amount of $HAuCl_4$, the size of Au@Ag@Au DSNPs presents an increasing trend from 22.86 to 25.41 nm, thus the Au shell thickness increases from 0.93 to 2.11 nm. In addition, the UV-vis spectroscopy is shown in Fig. S2B, in which the deposition of Au shell at the outer surface induces the successive red shift of LSPR peak at 502 nm with the Au shell getting thicker, and an intensity declines around 395 nm (curves c-f). Furthermore, the SERS signal of these prepared Au@Ag@Au DSNPs is proven to be modulated by the thicknesses of outer Au shell. As shown in Fig. S2C and S2D, the SERS intensity increases with increasing Au thickness and reaches the maximum when $HAuCl_4$ concentration is 15.8 μM. Thus, 15.8 μM $HAuCl_4$ concentration is chosen for the synthesis of Au@Ag@Au DSNPs.

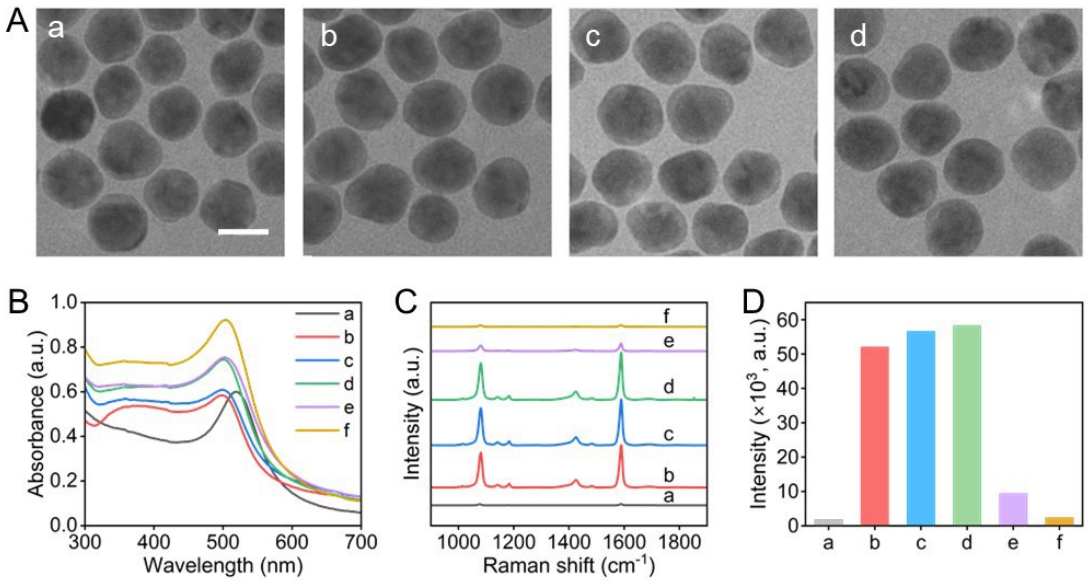

Fig. S2. (A) TEM images of Au@Ag@Au DSNPs synthesized with $HAuCl_4$ concentration of (a) 6.3, (b) 15.8, (c) 31.6, (d) 47.4 μM. (B) UV-vis absorption spectra and (C) SERS spectra of (a) Au NPs, (b) Au@Ag NPs prepared by 400 mM silver ammonium solution, and Au@Ag@Au DSNPs synthesized with $HAuCl_4$ concentration of (c) 6.3, (d) 15.8, (e) 31.6, and (f) 47.4 μM. (D) The corresponding SERS intensity from (C). The scale bar in (A): 20 nm.

S2.3. Elemental Mapping of Au@Ag@Au DSNPs.

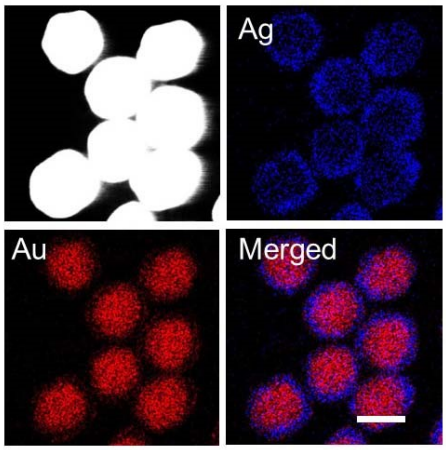

Fig. S3. Elemental mapping of Au@Ag@Au DSNPs. Scale bar: 20 nm.

S2.4. Stability of Au@Ag@Au DSNPs

The stability of Au@Ag@Au DSNPs was investigated by H_2O_2 etching, in which the Au@Ag NPs and Au@Ag@Au DSNPs were incubated in 10 mM H_2O_2 for 48 h, respectively. As shown in Fig. S4, the UV-vis spectrum of Au@Ag@Au DSNPs hardly changes before and after incubation. However, for Au@Ag NPs, the absorption peak at 395 nm corresponding to Ag completely disappears after incubation with H_2O_2, and the absorption peak of Au red-shifts from 502 to 518 nm, indicating the complete etching of Ag shell. Thus, the Au shell improves the stability of Au@Ag NPs and further reduces the toxicity induced by released Ag^+.

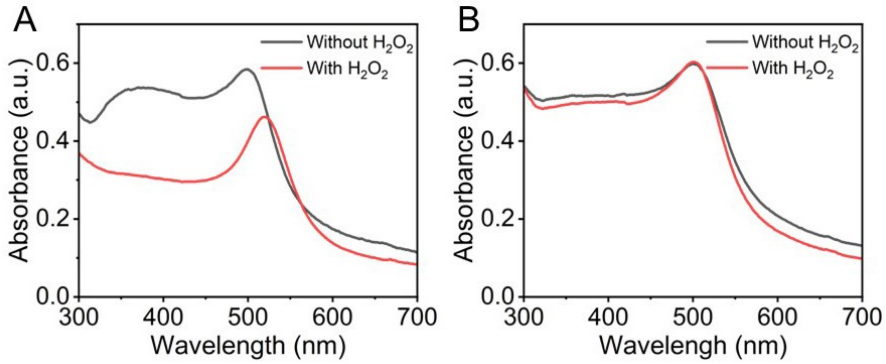

Fig. S4. Stability of (A) Au@Ag NPs and (B) Au@Ag@Au DSNPs before and after incubation with 10 mM H_2O_2 for 48 h.

S2.5. Quantification of HA Immobilized on Au@Ag@Au DSNPs

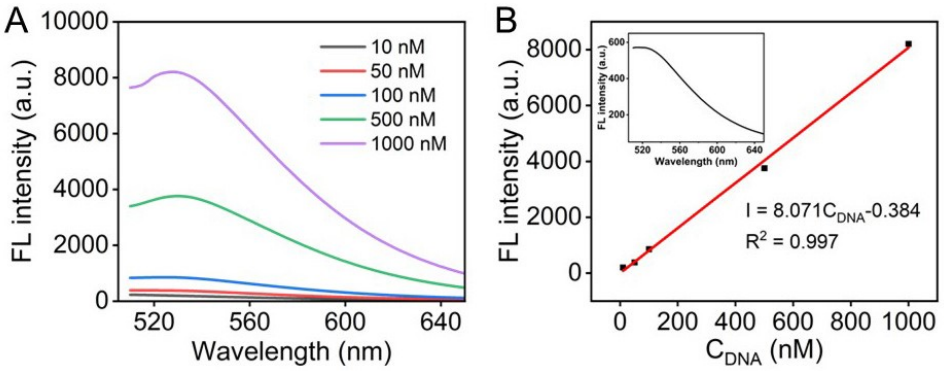

Fig. S5. (A) Fluorescence spectra and (B) corresponding standard curve of FAM-labelled HA hybrids with different concentrations. Inset in (B) presents the fluorescence spectra of HA-DSNPs after incubation with DTT.

S2.6. XPS Spectra of DKL-DND

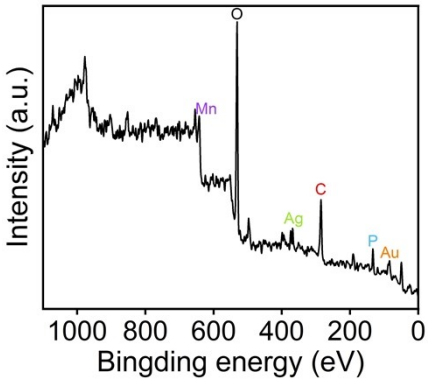

Fig. S6. XPS spectra of DKL-DND.

S2.7. Raman Spectra of DKL-DND

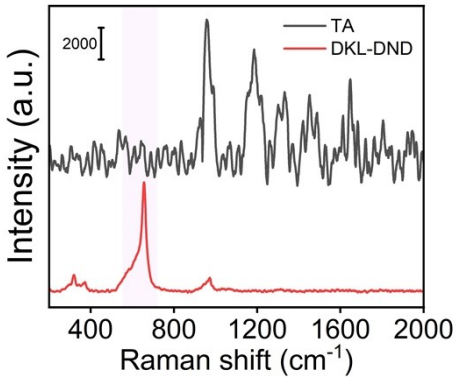

Fig. S7. Raman spectra of DKL-DND.

S2.8. DLS and ζ-potential Measurements of DKL-DND

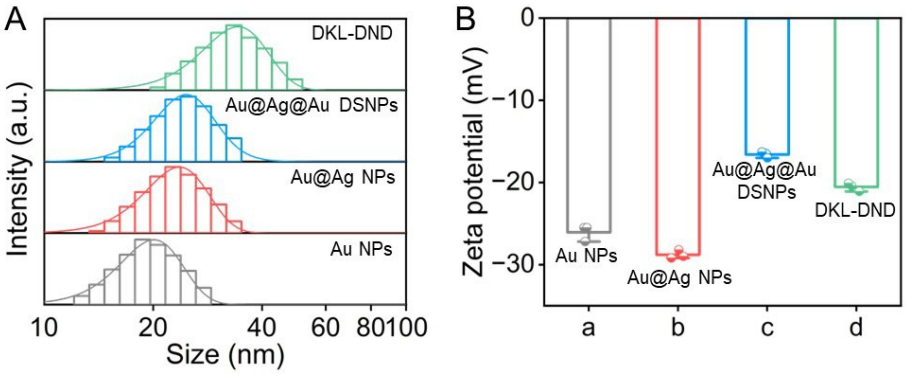

Fig. S8. (A) Hydrodynamic diameter and (B) ζ potential of AuNPs, Au@Ag NPs, Au@Ag@Au DSNPs, and DKL-DND. Error bars represent the standard deviation obtained from three independent assays.

S2.9. Stability Test of DKL-DND

The DKL-DND was treated with 10% FBS for different times to demonstrate its stability. There is almost no change in the particle size even after 24 h (Fig. S9A), indicating the good stability of DKL-DND. Furthermore, the fluorescence assay was carried out to verify whether the MOFs could protect DNA strands from enzymatic digestion, in which the fluorophore (Cy5) and quencher (BHQ2) were labelled at the proper sites of Fuel strand, and fluorophore (Rox) was labelled at the Aptazyme, respectively. As shown in Fig. S9B, the fluorescence recovery of Cy5 from DKL-DND is much lower than that of free Fuel strand in the presence of deoxyribonuclease I (DNase I, 1 U/mL). Meanwhile, Rox from DKL-DND shows the negligible fluorescence changes under the same conditions, indicating that the MOF shell could protect DNA strands from nuclease interference due to the steric hindrance effect between DNase I and DKL-DND.

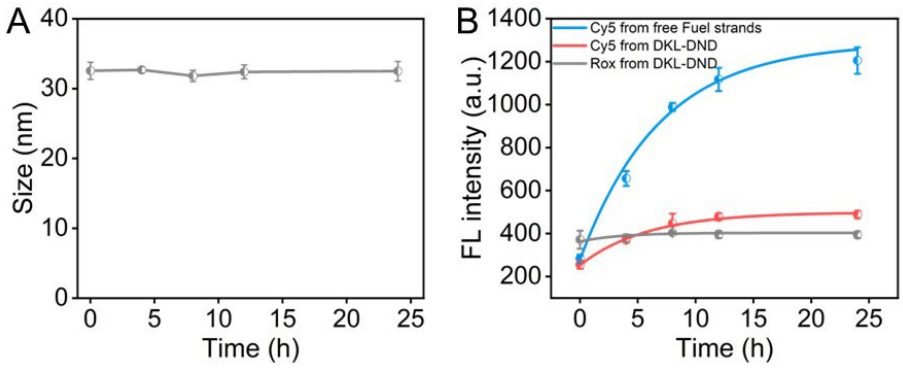

Fig. S9. (A) Particle sizes of DKL-DND in cell culturing medium containing 10% FBS at 37 °C at different times points. (B) Fluorescence analysis of DKL-DND after incubation with DNase I (1 U/mL) for 48 h. Error bars represent the standard deviation obtained from three independent assays.

S2.10. TEM Characterization of DKL-DND in PBS Buffer (pH 5.5)

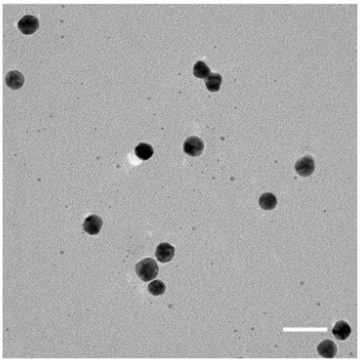

Fig. S10. TEM image of DKL-DND after incubation in PBS buffer (pH 5.5) for 4 h.

S2.11. Feasibility of DKL-DND for FL/SERS Detection of MiR-21

As shown in Fig. S11A, after the cascaded response of weakly acidic pH and ATP, the molecular switch of released Hairpin occurs a spontaneously conformational change to bring the miR-21 binding domains (toehold domain and branch migration domain) in close proximity. Upon the addition of miR-21, it hybridizes and docks to the toehold domain of Hairpin and subsequently opens the loop of Hairpin via an irreversible branch migration process, forming the Hairpin/miR-21 hybrid (step (1) and step (2)). Subsequently, the toehold domain of Fuel strand hybridizes with the newly exposed domain of Hairpin to open the loop of Fuel strand and simultaneously displace miR-21 from the Hairpin/miR-21 hybrid, resulting in the formation of Hairpin/Fuel (HF) complex. And the displaced miR-21 can catalyze another CHA process, achieving signal amplification (step (3) and step (4)).

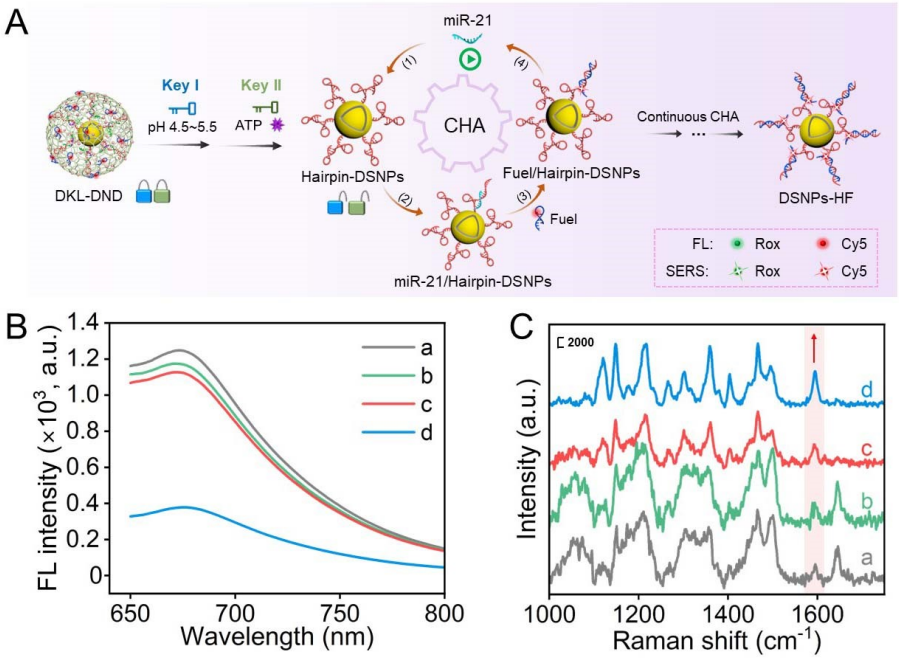

Fig. S11. (A) Principle of CHA for amplified detection of miR-21 after responding to acidic pH and ATP. (B) Fluorescence spectra and (C) SERS spectra of Cy5 obtained from the nanodevice (a) DKL-DND, (b) DKL-DND + miR-21 (50 nM), (c) DKL-DND + ATP (5 mM), and (d) DKL-DND + ATP (5 mM) + miR-21 (50 nM).

Taking advantage of distance dependent optical properties by Au@Ag@Au DSNPs, the feasibility of DKL-DND for FL/SERS dual-mode detection of miR-21 was investigated (Fig. S11B and S11C). The quenched fluorescence (675 nm) and enhanced SERS signal of Cy5 (1595 cm^{-1}) are readily observed when miR-21 exists under weakly acidic pH with 5 mM ATP, confirming that the DKL-DND works well for FL/SERS dual-mode detection of target microRNA.

S2.12. Native PAGE Characterization

The reaction pathways of CHA and Aptazyme-catalyzed cleavage were characterized by native PAGE. As shown in Fig. S12A, the lanes 1, 2 and 4 represent Aptazyme, Hairpin and Fuel strand, respectively. The new band corresponding to HA hybrid shows a slower migration compared to the monomers of Aptazyme and Hairpin (lane 3), indicating that the HA hybrid is indeed formed as designed. With the addition of ATP (5 mM), the Aptazyme can specifically bind with ATP through the exposed recognition site (16 bases), resulting in the disassembly of HA hybrids. Fuel strand and the released Hairpin could coexist metastably without miR-21 because they are kinetically trapped (lane 5). Also, the Hairpin is efficiently blocked by Aptazyme, in which miR-21 could not trigger the CHA process in the absence of ATP (lane 6). When the system contains HA hybrids, Fuel strand, miR-21 and ATP, an obvious band representing the HF hybrid is formed (lane 7), suggesting the successful operation of ATP-controlled CHA triggered by miR-21. Notably, the released Aptazyme is able to specifically cleave EGR-1 mRNA in the presence Mn^{2+} (lanes 8 and 9), demonstrating the feasibility of this system for Aptazyme-catalyzed gene silencing. Furthermore, the concentration of Mn^{2+} was investigated on Aptazyme-catalyzed cleavage reaction (Fig. S12B).

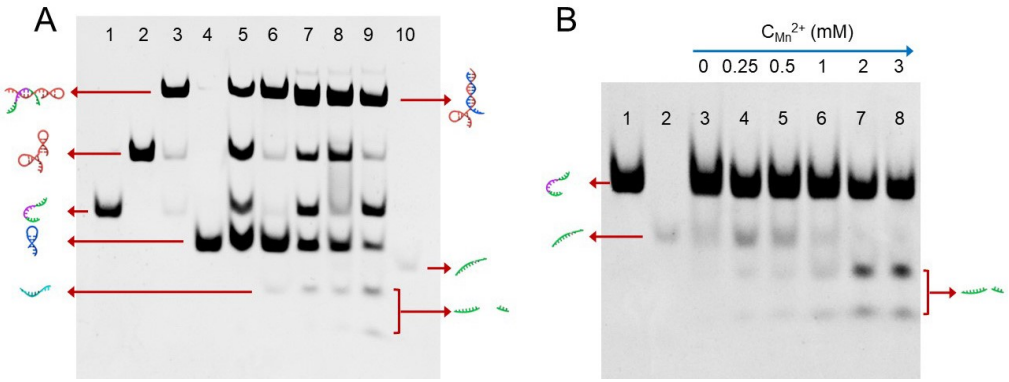

Fig. S12. Native PAGE characterization of (A) the reaction pathways of CHA and Aptazyme-catalyzed cleavage of EGR-1 mRNA and (B) the optimal concentration of Mn^{2+}. The pH of reaction system was adjusted to 7.4 using NaOH solution (0.5 M) to avoid the inference of ATP hydrolysis.

S2.13. Optimization of Reaction Time

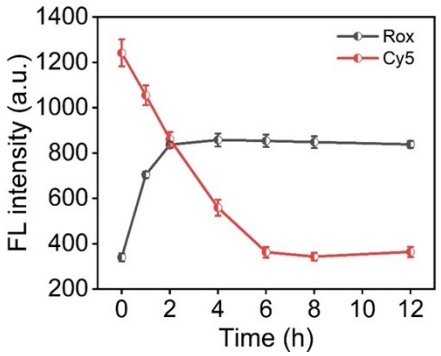

Fig. S13. Optimization of reaction time. Error bars represent the standard deviation obtained from three independent assays.

S2.14. *In Vitro* FL/SERS Detection of miR-21

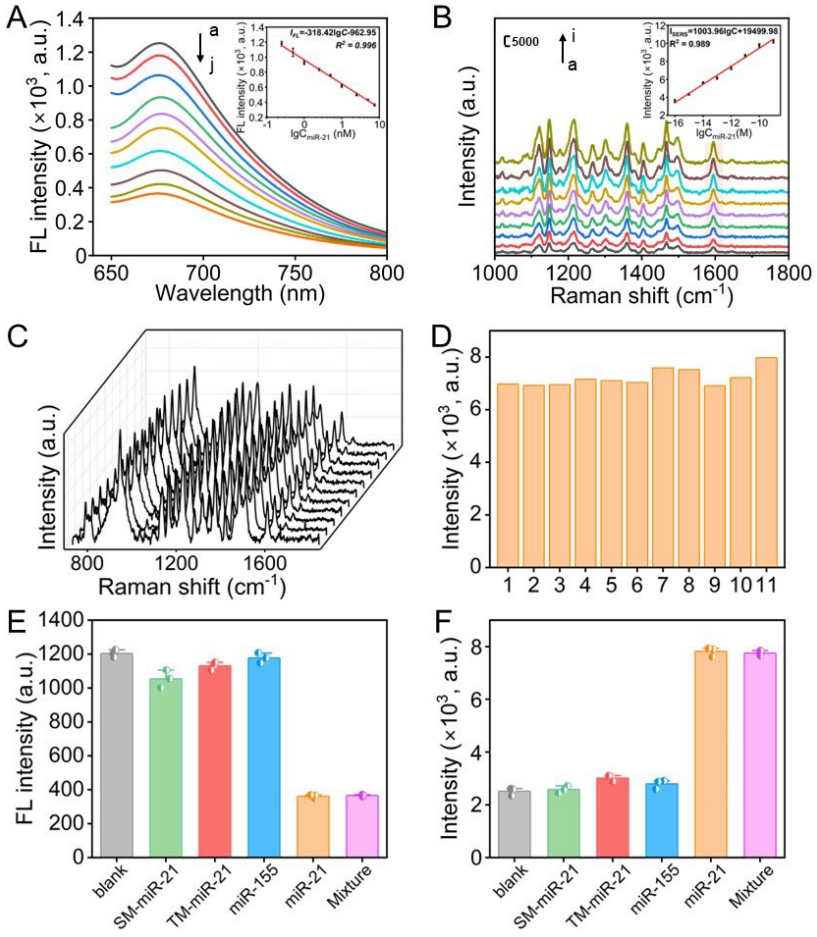

Fig. S14. (A) FL spectra of DKL-DND for the detection of miR-21 with various concentrations. Inset: the corresponding linear relationship between fluorescence intensity and logarithm of miR-21 concentration. From (a) to (j): 0 pM, 250 pM, 500 pM, 1 nM, 2.5 nM, 5 nM, 10 nM, 50 nM, and 75 nM miR-21. (B) SERS spectra of DKL-DND for the detection of miR-21 with various concentrations. Inset: the corresponding linear relationship between SERS intensity and logarithm of miR-21 concentration. From (a) to (i): 0 fM, 0.1 fM, 1 fM, 10 fM, 100 fM, 1 pM, 10 pM, 100 pM, and 1 nM miR-21. (C) SERS spectra for detection of miR-21 (1 pM) using DKL-DND (2.5 nM) and (D) corresponding SERS intensities at 1595 cm^{-1} obtained from (C). Eleven random spots were chosen on the same substrate. Specificity of DKL-DND (2.5 nM) for miR-21 detection (50 nM) using (E) FL mode and (F) SERS mode, respectively. Error bars represent the standard deviation obtained from three independent assays.

S2.15. Anti-Interference Ability of DKL-DND

To evaluate the anti-interference ability, DKL-DND was pre-treated with MCF-7 cell lysate for different times. Then, the collected DKL-DND was used to detect miR-21 (100 pM) by SERS mode. As shown in Fig. S15, almost no change in SERS intensity is observed compared with the control group without treatment, indicating the excellent anti-interference ability of DKL-DND.

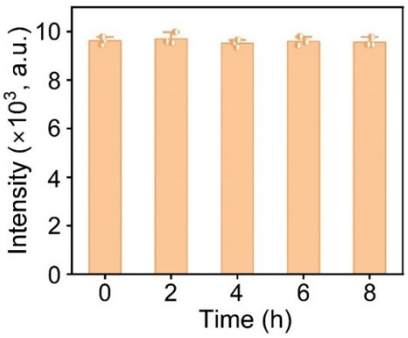

Fig. S15. Anti-interference ability of DKL-DND (2.5 nM) for detection of miR-21 (100 pM). Error bars represent the standard deviation obtained from three independent assays.

S2.16. Flow Cytometry Assay

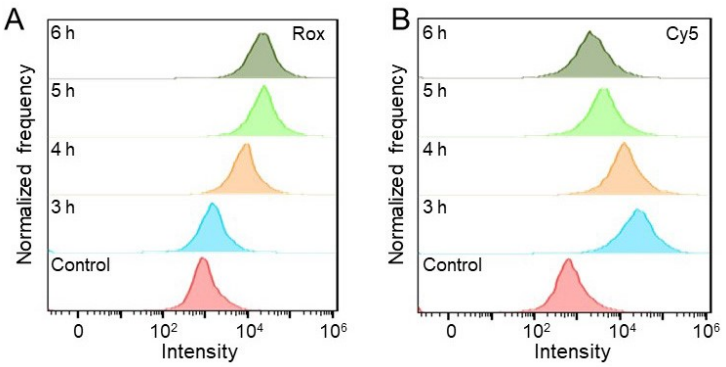

Fig. S16. Flow cytometry results of (A) Rox and (B) Cy5 from DKL-DND (5 nM) after incubation with MCF-7 cells.

S2.17. Evaluation of Intracellular miR-21 Expression Levels

To monitor the relative dynamic change of microRNA expression level in living cells, MCF-7 cells were pre-incubated with miR-21 mimics and miR-21 inhibitor to upregulate and downregulate the expression of miR-21, respectively. After incubation with DKL-DND for 6 h, no fluorescence signal of Cy5 is observed for miR-21 mimics-pretreated MCF-7 cells, whereas a much more intense red fluorescence is recorded for miR-21 inhibitor-pretreated cells. Thus, the fluorescence readout in DKL-DND is closely related to miR-21 concentration, which is able to well monitor the varied expressions of intracellular microRNAs.

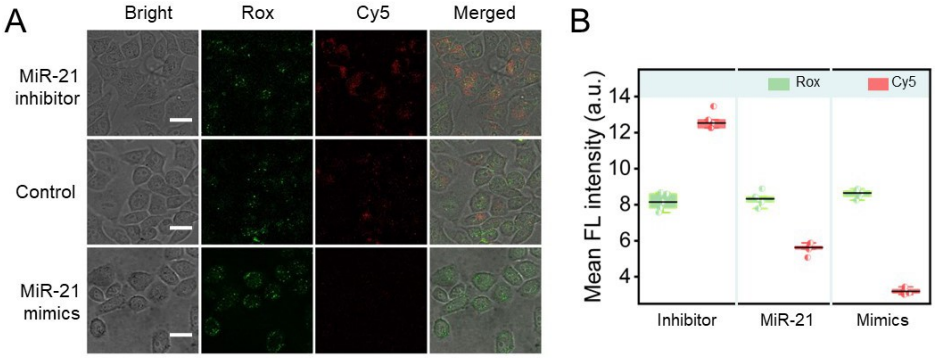

Fig. S17. (A) CLSM images and (B) corresponding fluorescence intensity of MCF-7 cells pretreated with miR-21 inhibitors, PBS, and miR-21 mimics, followed by incubation with DKL-DND (5 nM), respectively. Error bars represent the standard deviation obtained from three independent assays. Scale bar: 25 μm.

S2.18. Concentrations of ATP in Different Cell Lines

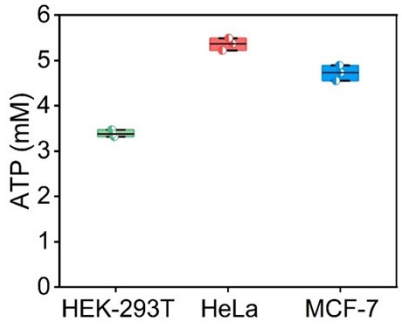

Fig. S18. ATP concentrations of three cell lines (HEK-293T, HeLa and MCF-7 cells) qualified by ATP assay kit. Error bars represent the standard deviation obtained from three independent assays.

S2.19. Relative miR-21 Expression in Different Cell Lines

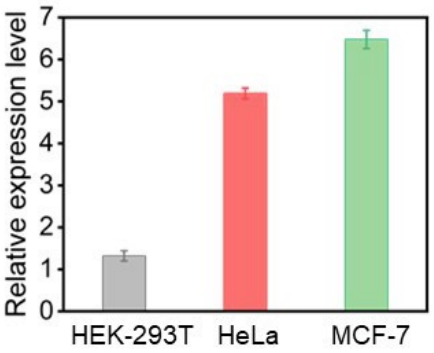

Fig. S19. Quantification of relative miR-21 expression in different cell lines using qRT-PCR. Error bars represent the standard deviation obtained from three independent assays.

S2.20. SERS Spectra Obtained from Different Positions

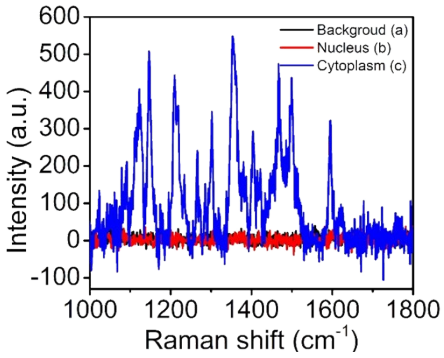

Fig. S20. SERS spectra at different positions of MCF-7 cells: (a) the surrounding environment, (b) cell nucleus, and (c) cytoplasm.

S2.21. Dox Loading and Release Capacity of DKL-DND

First, the drug loading capacity was determined by fluorescence assay, in which 20 μM Dox was incubated with different concentrations of HA-DSNPs for 24 h. From Fig. S21A and S21B, the fluorescence intensity of Dox gradually decreases with the increasing amounts of HA-DSNPs, demonstrating the successful intercalation of Dox, and the molar ratio of HA-DSNPs to loaded Dox was assessed to be 1:400. Furthermore, the release efficiency of DKL-DND was evaluated at different conditions (Fig. S21C). The DKL-DND displays a negligible release behavior after incubation in the reaction buffer (pH 5.5) for 24 h. Upon incubation with ATP and miR-21, the release efficiency of Dox is further enhanced and reached to ~70.79%, proving the disassembly of DNA duplexes facilitates drug release.

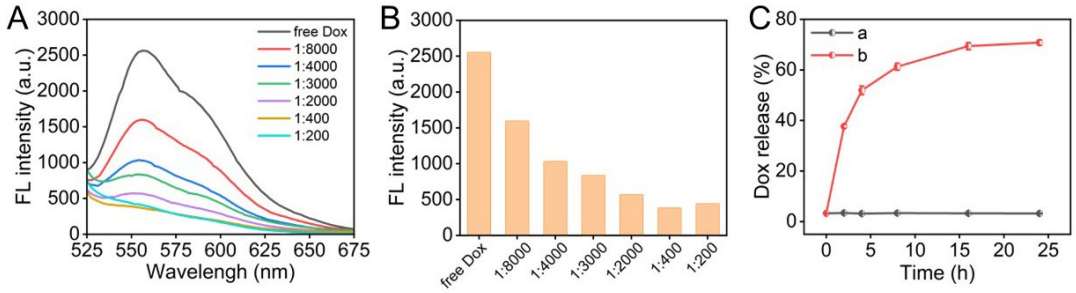

Fig. S21. (A) Fluorescence spectra and (B) corresponding fluorescence intensity of Dox with increasing the amounts of HA-DSNPs. (C) Drug release efficiency of DKL-DND after incubation with (curve a) or without (curve b) ATP (5 mM) and miR-21 (50 nM) in the reaction buffer (pH 5.5) for 24 h. Error bars present the standard deviation obtained from three independent assays.

S2.22. Migration Ability of MCF-7 cells

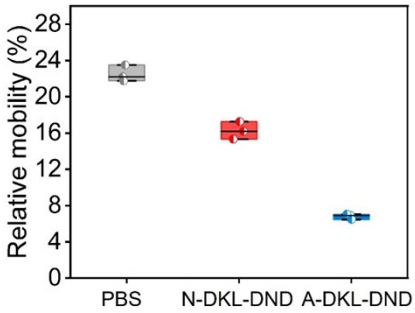

Fig. S22. Relative mobility of MCF-7 cells at 24 h after different treatments.

S2.23. Hemolysis Assay

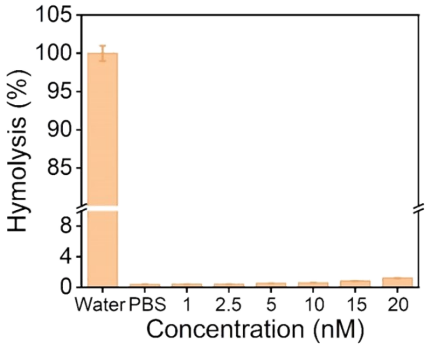

Fig. S23. Hemolysis analysis of red blood cells treated with water, PBS and N-DKL-DND (from 1 to 20 nM), respectively. Error bars represent the standard deviation obtained from three independent assays.

S2.24. Dynamic Accumulation Behaviors of DKL-DND in Tumor Site

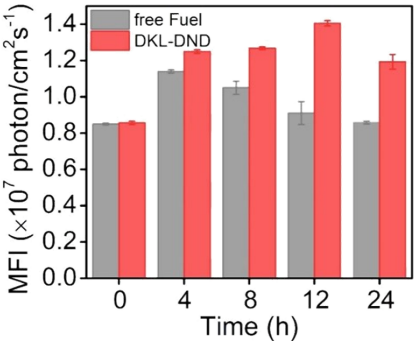

Fig. S24. Mean fluorescence intensity of tumors treated with free Fuel strand and DKL-DND at different time points, respectively. Error bars represent the standard deviation obtained from three independent assays.

S2.25. *Ex Vivo* Fluorescence Imaging of Organs and Tumors

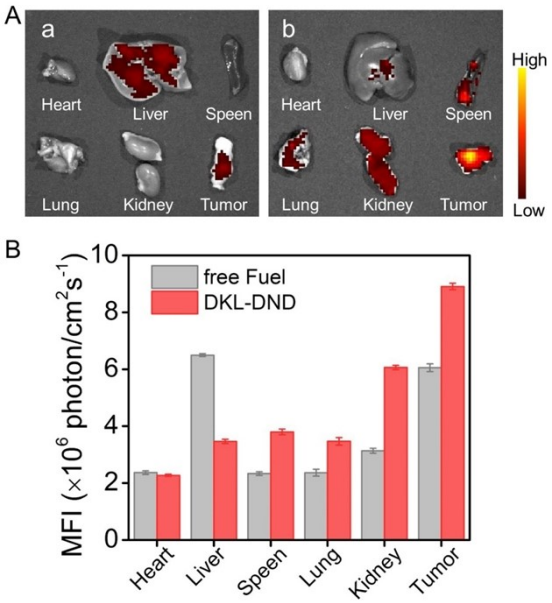

Fig. S25. (A) *Ex vivo* fluorescence imaging of main organs and tumors treated with (a) free Fuel strand and (b) DKL-DND, respectively. (B) Corresponding mean fluorescence intensity of (A). Error bars represent the standard deviation obtained from three independent assays.

S2.26. Biodistribution and Pharmacokinetics of DKL-DND

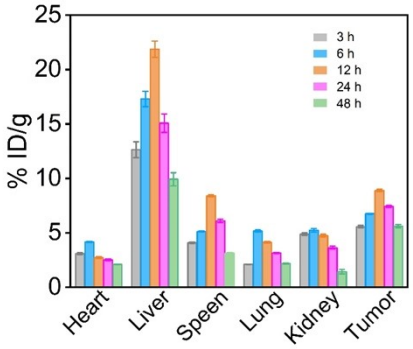

Fig. S26. Biodistribution of DKL-DND in main organs at different time points post-injection. Error bars represent the standard deviation obtained from three independent assays.

S2.27. Body-Weight of Mice During Therapy

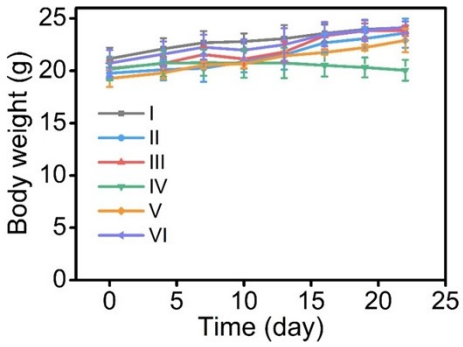

Fig. S27. Body-weight evolution curves during therapy with different treatments: (I) PBS, (II) N-DKL-DND, (III) A-DKL-DND, (IV) free Dox, (V) D-DKL-DND, and (VI) DKL-DND.

S2.28. Western Blot Analysis of Tumor samples

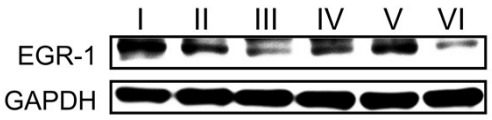

Fig. S28. Western blot assay of EGR-1 protein expressed in tumor tissue. From I to VI: (I) PBS, (II) N-DKL-DND, (III) A-DKL-DND, (IV) free Dox, (V) D-DKL-DND and (VI) DKL-DND.

S2.29. H&E Staining of Major Organs from Mice

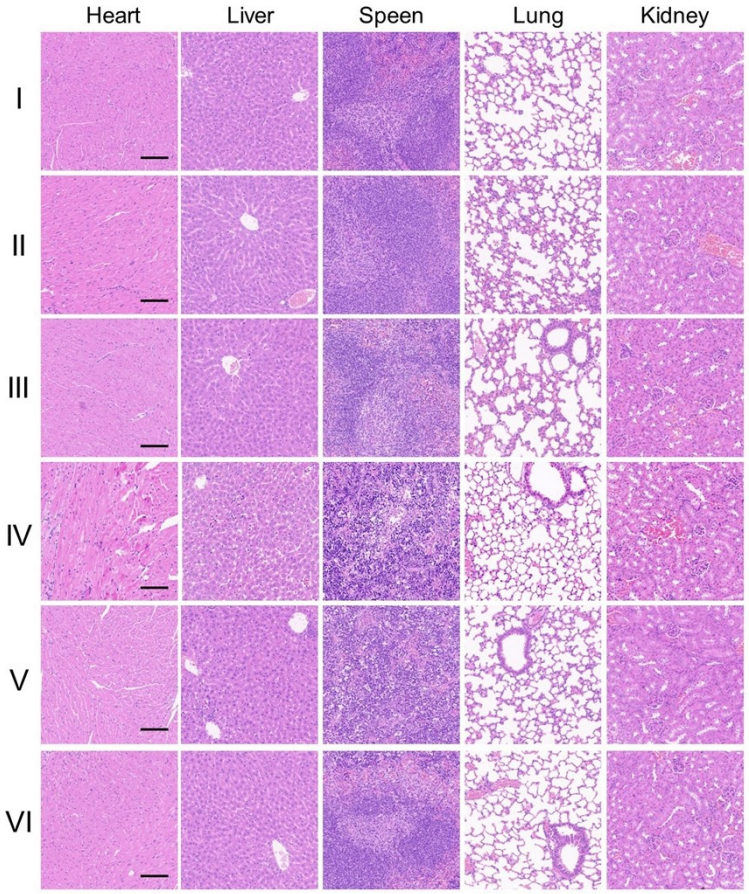

Fig. S29. H&E histological staining of major organs including heart, liver, spleen, lung, and kidney from the mice treated with (I) PBS, (II) N-DKL-DND, (III) A-DKL-DND, (IV) free Dox, (V) D-DKL-DND, and (VI) DKL-DND by the end of the 22th day. Scale bars: 100 μm.

S2.30. Blood Biochemistry Analysis

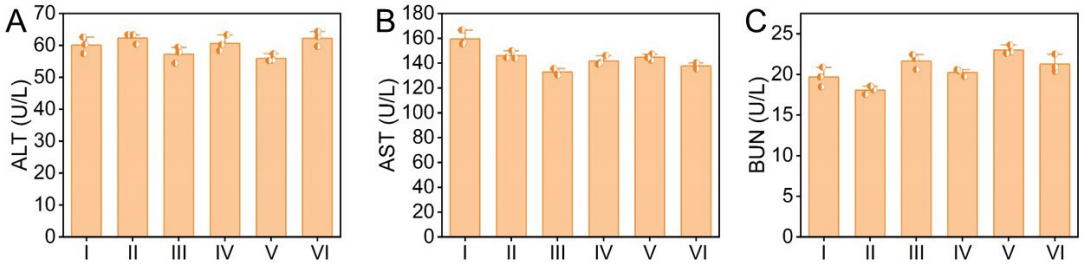

Fig. S30. Blood biochemistry analysis to evaluate the hepatic (A and B) and renal (C) functions of mice treated with (I) PBS, (II) N-DKL-DND, (III) A-DKL-DND, (IV) free Dox, (V) D-DKL-DND, and (VI) DKL-DND by the end of the 22th day. Error bars represent the standard deviation obtained from three independent assays.

Table S1. Oligonucleotide sequences used in this work.

Name	Sequence (5'-3')[a]
miR-21	UAGCUUAUCAGACUGAUGUUGA
one-base mismatched miR-21	UA**U**CUUAUCAGACUGAUGUUGA
three-base mismatched miR-21	UA**UA**UUAU**A**AGACUGAUGUUGA
miR-155	UUAAUGCUAAUCGUGAUAGGGGU
SH-Hairpin	C6-SH-TCAACATCCCACTCCTCCCCCAGGTAGCTAGCAGGAGTGGAGTCTGATAAGCTAATATGTGTAGATAGCTTATCAGACT
Aptazyme	CCGCGGCCAGGCTAGCTACCTGGGGGAGTATTGCGGAGGAAGGTACAACGACCTGGACGA
Rox-Aptazyme	CCGCGGCCAGGCTAGCTACCTGGGGGAGT/Rox/ATTGCGGAGGAAGGTACAACGACCTGGACGA
catalytically inactive Aptazyme	CCGCGGCCAGGCTA**C**CTACCTGGGGGAGTATTGCGGAGGAAGGTACAACGACCTGGACGA
Fuel	TAAGCTATCTACACATATTAGCTTATCAGACTATATGTGTAGA
Cy5-Fuel	TAAGCTATCTACACATATTAGCTTATCAGACT/Cy5/ATATGTGTAGA
Fuel*	TAAGCTATCTACACATATT/BHQ2/AGCTTATCAGACT/Cy5/ATATGTGTAGA
Substrate (EGR-1 mRNA)	TCGTCCAGG/rA//rU/GGCCGCGGTTTTTTTT
anti-miRNA-21	UCAACAUCAGUCUGAUAAGCUA
EGR-1 primers	(forward) TGACCGCAGAGTCTTTTCCT (reverse) TGGGTTGGTCATGCTCACTA
GAPDH primers	(forward) TGGGTGTGAACCATGAGAAGT (reverse) TGAGTCCTTCCACGATACCAA

[a]The mismatched bases are marked by bold and underline.

Table S2. Comparison of this work with other biosensors for microRNAs detection.

Method	Target	Linear range	Detection limit	Ref.
CRISPR/Cas13a powered portable ECL chip	miRNA-17	1 fM-0.1 nM	1 fM	[1]
HCR-based FL sensor	miRNA-155	1 nM-100 nM	680 pM	[2]
Endogenous enzyme-powered DNA nanomotor	miRNA-10b	50 pM - 50 nM	38.9 pM	[3]
dual-signal mode ratiometric photoelectrochemical sensor	miRNA-210	10 fM-1 nM	3 fM	[4]
DNA structure-stabilized SERS matrices	miRNA-155	100 fM-5 nM	1.45 fM	[5]
biomimetic array assay integrating luminescent CuNCs with entropy-driven nanomachine	miRNA-21	10 pM-50 nM	4.5 pM	[6]
DKL-DND-based dual mode sensor	miRNA-21	250 pM - 75 nM (FL) 0.1 fM - 1 nM (SERS)	0.74 pM (FL) 0.14 aM (SERS)	this work

References

1. T. Zhou, R. Huang, M. Huang, J. Shen, Y. Shan and D. Xing, *Adv. Sci.*, 2020, **7**, 1903661.
2. F. Yang, Y. Cheng, Y. Cao, H. Dong, H. Lu, K. Zhang, X. Meng, C. Liu and X. Zhang, *Chem. Sci.*, 2019, **10**, 1709-1715.
3. T. Li, M. Sun, Q. Zhou, P. Liang, T. Huang, M. Guo, B. Xie, C. Li, M. Li, W.-J. Duan, J.-X. Chen, Z. Dai and J. Chen, *Anal. Chem.*, 2023, **95**, 15025-15032.
4. J. Li, C. Chen, F. Luo, C. Lin, Z. Lin, J. Wang and B. Qiu, *Anal. Chem.*, 2023, **95**, 17670-17678.
5. C.-j. Wu, S.-q. Huang, Y.-y. Wang, Y.-q. Chai, R. Yuan and X. Yang, *Anal. Chem.*, 2021, **93**, 11019-11024.
6. C. Zhang, M. Wu, S. Hu, S. Shi, Y. Duan, W. Hu and Y. Li, *Anal. Chem.*, 2023, **95**, 11978-11987.